CHALMERS

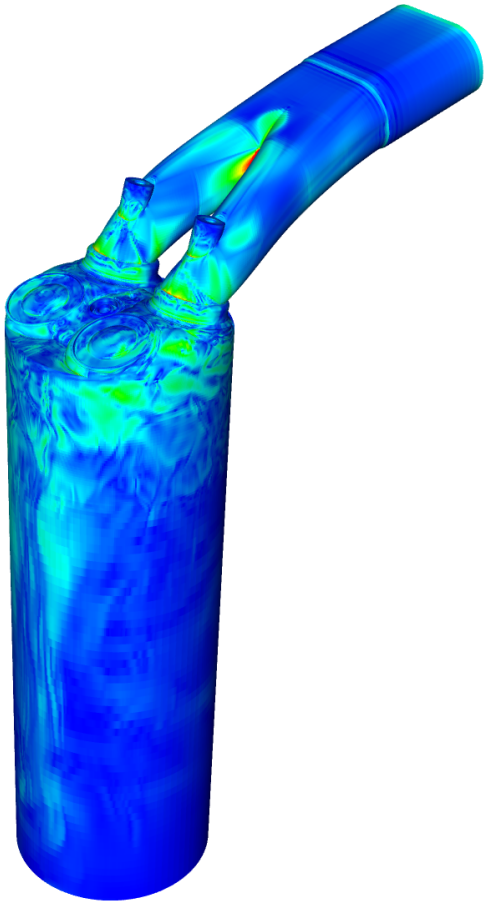

Predictions of the Flow in the Intake Port of an Engine Using LES and PANS

Master's Thesis in Applied Mechanics

TOBIAS EIDEVÅG MARTIN LINDSTRÖM

Department of Applied Mechanics
Division of Fluid Mechanics
CHALMERS UNIVERSITY OF TECHNOLOGY
Göteborg, Sweden 2013
Master's Thesis 2013:65

MASTER'S THESIS 2013:65

Predictions of the Flow in the Intake Port of an Engine Using LES and PANS

Master's Thesis in Applied Mechanics

TOBIAS EIDEVÅG MARTIN LINDSTRÖM

Department of Applied Mechanics
Division of Fluid Mechanics
CHALMERS UNIVERSITY OF TECHNOLOGY
Göteborg, Sweden 2013

Predictions of the Flow in the Intake Port of an Engine Using LES and PANS
TOBIAS EIDEVÅG MARTIN LINDSTRÖM

Master's Thesis 2013:65
ISSN 1652-8557
Department of Applied Mechanics
Division of Fluid Mechanics
Chalmers University of Technology
SE-412 96 Göteborg
Sweden
Telephone: + 46 (0)31-772 1000

Cover:
Spatial resolution in terms of the viscous unit n^+ for PANS.

Chalmers Reproservice
Göteborg, Sweden 2013

Predictions of the Flow in the Intake Port of an Engine Using LES and PANS
Master's Thesis in Applied Mechanics
TOBIAS EIDEVÅG MARTIN LINDSTRÖM
Department of Applied Mechanics
Division of Fluid Mechanics
Chalmers University of Technology

Abstract

The airflow in the cylinder of a car engine is simulated using three different techniques. Large Eddy Simulations (LES), Partially Averaged Navier-Stokes (PANS) and Reynolds Averaged Navier-Stokes (RANS). The simulations are compared with experimental data from BMW and a benchmark designed by BMW, executed by AVL List GmbH among others. A comparison and evaluation between the three different turbulence models is made, especially differences in flow physics. The study focuses on evaluting PANS for this complex geometry as well as understanding the tumble creation in the cylinder. The computational mesh was created using ANSYS ICEM CFD and the simulations were performed with AVL FIRE.

Keywords: Computational Fluid Dynamics (CFD), AVL FIRE, ICEM CFD, Partially Averaged Navier-Stokes (PANS), Large Eddy Simulation (LES), Intake Port, ζ - f, Turbulence model

Preface

In this study the flow in the intake port of an engine was simulated and analyzed using three different methods, Large Eddy Simulations (LES), Partially Averaged Navier-Stokes (PANS) and Reynolds Averaged Navier-Stokes (RANS). The result from the simulations were compared with experimental data using two key indicators. ANSYS ICEM CFD was used for mesh creation and the simulations were run in AVL FIRE. The study took place at the Department of Applied Mechanics, Division of Fluid Dynamics, Chalmers University of Technology, Sweden from January to August 2013, supported by AVL List GmbH and under the supervision of Professor Siniša Krajnović.

Acknowledgments

We would like to thank our supervisor Professor Siniša Krajnović for his supervision, expert help and support. We would also like to thank SNIC (Swedish National Infrastructure for Computing) for access to their resources. Furthermore, we want to thank AVL List GmbH for providing FIRE licenses and especially to Doctor Branislav Basara for his technical support with both the project as well as with the FIRE code.
We want to thank Jan Östh for teaching us how to create a mesh in ICEM CFD, for helping us with our simulation settings, for his fast replies to emails and for always being so friendly. We would also like to acknowledge the rest of the faculty members at the Division for their help and support.
Finally we would like to thank our friends and families for their never ending support, especially to our girlfriends Emily Lindberg and Karin Jensen for putting up with the long days at Chalmers.

Göteborg August 2013
Tobias Eidevåg Martin Lindström

Nomenclature

Abbrevations

CFD	Computational Fluid Dynamics
CFL	Courant Friedrichs Lewy
DNS	Direct Numerical Simulation
LES	Large Eddy Simulation
MPI	Message Passing Interface
PANS	Partially Averaged Navier-Stokes
RANS	Reynolds Averaged Navier-Stokes
SGS	Sub Grid Scale
URF	under-relaxation factor

Greek Letters

Δ	Filter width
Δt	Time step
Δx, Δy, Δz	Cell sizes
δ_{ij}	Kronecker delta
ε	Dissipation
γ	Heat capacity ratio for air
Λ	Kolmogorov scale of turbulence
μ	Dynamic viscosity
ν_{sgs}	Sub grid scale viscosity
ν_u	Turbulent viscosity
ρ_b	Static density
ρ	Density
ρ_i	Static density at face area i
ρ_{out}	Area averaged static density at outlet

$\sigma_{k,\varepsilon,\zeta}$	Coefficients in the PANS model
$\sigma_{A_s,TU}$	Standard deviation of A_s and TU
τ_{ij}	Sub grid scale stress tensor
τ_w	Wall shear stress
ζ	Velocity scale ratio

Roman Letters

$A_{i,n}$	Area of face i of plane n
A_{ref}	Reference cross section
C	Courant number
$C^*_{\varepsilon 1}$, $C^*_{\varepsilon 2}$, c_1, C'_2	Coefficients in the PANS model
C_S	Smagorinsky constant
C_μ, $C_{\varepsilon 1}$, $C_{\varepsilon 2}$, C_{f1}	Constans in the $\zeta - f$ model
C_{f2}, C_τ, C_L, C_ν	Constans in the $\zeta - f$ model
D	Bore diameter
f	Elliptic relaxation function
f_ε	Unresolved-to-total ratio of dissipation
f_k	Unresolved-to-total ratio of kinetic energy
k	Turbulent kinetic energy
L	Length scale
$\dot{m}_{real}$	Mass flow rate at inlet
$\dot{m}_{theory}$	Isentropic mass flow rate
$M_{x,n}$	Torque around the x-axis of plane n
n	Wall normal distance
l^+	Viscous unit, stream-wise direction
n^+	Viscous unit, wall normal direction
s^+	Viscous unit, orthogonal to n and l
$\bar{p}$	Filtered pressure
P	Production term
p_{cyl}	Average pressure in cylinder
p_{in}	Total pressure at inlet

p_{tot}	Total pressure
R_{gas}	Gas constant of air
$\bar{S}_{ij}$	Resolved rate of strain
T	Time scale
T_{in}	Temperature at inlet
TU_n	Tumble number at plane n
$\bar{u}$	Filtered veolcity in LES
u^*	Friction velocity
u_x, u_y, u_z	Velocity in x-, y- and z-directions
$\dot{V}$	Volumetric flow rate at outlet
w_i	Velocity component in z-direction at the center of face i
Y_i	y-coordinate of center of face i

Contents

Chapter 1

Introduction

A short background and motivation why the subject is of interest is given along with the previous work done on the subject. The purpose and the delimitations of the study are presented. At the end of the chapter there is a short summary of the approach used in order to obtain the results.

1.1 Background and Previous Work

The efficiency of an internal combustion engine for an automobile is closely related to the air-fuel-mixing in the cylinder, the better the mix, the higher the efficiency. Higher efficiancy in an internal combustion engine is closely related to a decrease in carbon dioxide emmisions and is thus important for a sustainable developement. The air-fuel-mixing in the cylinder is related to the flow in the intake port and especially the swirl and tumble caused by the flow. Thus, the prediction and understanding of the flow in the intake port is essential for improvement of the engine design.
Experiments to measure the flow of an intake port are rarely performed due to practical limitations in what can be measured. Global quantities such as tumble can be measured but the results of these experiments are usually confidential, making the validation of numerical simulations difficult. However, in October 2011 an experimental study [9] performed by BMW was made public to the scientific community. A benchmark, designed by BMW [7], to simulate the experiment was given to AVL List GmbH among others but the agreement with the experiments were poor. AVL List GmbH did their simulations using Reynolds Averaged Navier-Stokes (RANS) equations with an eddy viscosity model.

1.2 Purpose

The purpose of this study is to gain knowledge of the complex flow physics of an intake port. This was done by running simulations using three different methods, namely RANS (Reynolds Averaged Navier-Stokes), LES (Large Eddy Simulations) and PANS (Partially Averaged Navier-Stokes). LES is supposed to be the most accurate model although PANS has been proven to perform better then LES on a coarser mesh [3, 10, 11]. A secondary objective of the study is to evalute PANS for this geometry.

1.3 Delimitations

It is important to note that the experiments were carried out on a geometry with no moving parts, hence there are no moving parts in this study. The flow is analyzed with

the invalve at 2 different levels; 6 mm and 10 mm. There are experiments with the invalve at 2 mm as well but due to the limited time frame, this third level is not covered in the report. The experiments were made with only air and no fuel and thus, the mixing of only air will be modeled in this study. The effects of multiphase interaction between fuel and air is then not taken into account so the flow predictions will only be depending on the geometry. Furthermore, it should also be noted that the given geometries had to be very slightly adjusted in order for a computational grid to be created. It is however the belief of the authors that these adjustments affect the result less then the unavoidable geometry changes made due to the fact that a computational grid can not resolve a complex geometry perfectly.
The experiments were carried out using two slightly different geometries but because of the finite time frame of this study, only one of the geometries will be examined. The flow is modeled as incompressible because of its low velocities and in order to simplify the models. It should also be mentioned that this study does in no way attempt to improve or even suggest improvements of the geometry.

1.4 Approach

The geometries were provided by AVL List GmbH. Using ANSYS ICEM CFD the geometries were cleaned and prepared for meshing. A structured hexahedral computational grid was created using ANSYS ICEM CFD and thereafter the grid was mirrored around the symmetry plane. On this grid, simulations were performed with AVL FIRE and the results were then visualized in Ensight. The results were further analyzed through various plots created in MATLAB.

Chapter 2

Theory

In this study, simulations were carried out using three different models, namely LES, PANS and RANS. This chapter presents the equations behind the models. The requirements on the computational grid is stated and the key indicators used to analyze the result are presented.

2.1 LES - Large Eddy Simulations

The idea behind Large Eddy Simulations (LES) is to resolve the large energy containing eddies and model the effect of the smaller dissipative eddies. The Naiver-Stokes equations are spatially filtered using the grid as a filter. Large eddy scales i.e. scales larger than the grid is therefore solved explicitly and small scales is modeled by a subgrid-scale model. In this study, the subgrid-scale model of choice is the standard Smagorinsky model [13] with a wall damping function. The governing equations for incompressible flow are the continuity equation and the momentum equations, together forming the Navier-Stokes equations. Filtering these equations yield

$$\frac{\partial \bar{u}_i}{\partial x_i} = 0 \tag{2.1.1}$$

$$\frac{\partial \bar{u}_i}{\partial t} + \frac{\partial}{\partial x_j}\left(\bar{u}_i \bar{u}_j\right) = -\frac{1}{\rho}\frac{\partial \bar{p}}{\partial x_i} + \nu \frac{\partial^2 \bar{u}_i}{\partial x_j \partial x_j} - \frac{\partial \tau_{ij}}{\partial x_j} \tag{2.1.2}$$

where $\tau_{ij} = \overline{u_i u_j} - \bar{u}_i \bar{u}_j$ is the residual stress tensor or Sub Grid Scale (SGS) stress tensor. Using the standard Smagorinsky model it is modeled as

$$\tau_{ij} - \frac{1}{3}\delta_{ij}\tau_{kk} = -\nu_{sgs}\left(\frac{\partial \bar{u}_i}{\partial x_j} + \frac{\partial \bar{u}_j}{\partial x_i}\right) = -2\nu_{sgs}\bar{S}_{ij} \tag{2.1.3}$$

$$\nu_{sgs} = \left(C_S \Delta\right)^2 \sqrt{2\bar{S}_{ij}\bar{S}_{ij}} \equiv \left(C_S \Delta\right)^2 \left|\bar{S}\right| \tag{2.1.4}$$

where ν_{sgs} is the sub grid scale viscosity, $\bar{S}_{ij}$ the resolved rate of strain and the filter width $\Delta = V_{ijk}^{1/3}$, where V_{ijk} is the volume of cell ijk [4].

2.2 RANS - Reynolds Averaged Navier-Stokes

Reynolds Averaged Naiver-Stokes (RANS) is a timeaveraged formulation of the Naiver-Stokes equations. With this formulation a turbulence model is then applied. The turbulence model chosen in this study is the $\zeta - f$ model developed by Hanjalić et al [8]. The

$\zeta - f$ model is based on the $\bar{v^2} - f$ model by Durbin [5] as a more robust alternative. Where the velocity scale ratio $\zeta = \overline{v^2}/k$. The complete $\zeta - f$ model is given below.
The turbulence viscosity is defined as

$$\nu_t = C_\mu \zeta k \tau \tag{2.2.1}$$

and the transport equations are

$$\frac{\partial k}{\partial t} + \bar{u}_j \frac{\partial k}{\partial x_j} = \frac{1}{\rho}\frac{\partial}{\partial x_j}\left[\left(\mu + \frac{\mu_t}{\sigma_k}\right)\frac{\partial k}{\partial x_j}\right] + P_k - \varepsilon \tag{2.2.2}$$

$$\frac{\partial \varepsilon}{\partial t} + \bar{u}_j \frac{\partial \varepsilon}{\partial x_j} = \frac{1}{\rho}\frac{\partial}{\partial x_j}\left[\left(\mu + \frac{\mu_t}{\sigma_\varepsilon}\right)\frac{\partial \varepsilon}{\partial x_j}\right] + \frac{1}{\tau}[C^*_{\varepsilon 1} P_k - C_\varepsilon \varepsilon] \tag{2.2.3}$$

$$\frac{\partial \zeta}{\partial t} + \bar{u}_j \frac{\partial \zeta}{\partial x_j} = \frac{1}{\rho}\frac{\partial}{\partial x_j}\left[\left(\mu + \frac{\mu_t}{\sigma_\zeta}\right)\frac{\partial \zeta}{\partial x_j}\right] + f - P_k \frac{\zeta}{k} \tag{2.2.4}$$

where f is a damping function, defined as

$$L^2 \frac{\partial^2 f}{\partial x_j \partial x_j} - f = \left(C_{f1} + C_{f2}\frac{P_k}{\varepsilon}\right)\left(\zeta - \frac{2}{3}\right)\frac{1}{\tau} \tag{2.2.5}$$

L and τ are the turbulent length- and time scales respectively, given by

$$\tau = max\left[min\left[\frac{k}{\varepsilon}, \frac{0.6}{\sqrt{6}C_\mu |S| \zeta}\right], C_\tau \left(\frac{\nu}{\varepsilon}\right)^{1/2}\right] \tag{2.2.6}$$

$$L = C_L max\left[min\left[\frac{k^{3/2}}{\varepsilon}, \frac{\sqrt{k}}{\sqrt{6}C_\mu |S| \zeta}\right], C_\eta \left(\frac{\nu^3}{\varepsilon}\right)^{1/4}\right] \tag{2.2.7}$$

The coefficients used in the $\zeta - f$ model can be found in table 2.2.

Table 2.2.1: Coefficients used in the $\zeta - f$ model.

C_μ	$C^*_{\varepsilon 1}$	$C_{\varepsilon 1}$	$C_{\varepsilon 2}$	C_{f1}	C_{f2}	σ_k	σ_ε	σ_ζ	C_τ	C_L	C_ν
0.22	$C_{\varepsilon 1}(1 + 0.012/\zeta)$	1.4	1.9	0.4	0.65	1	1.3	1.2	6	0.36	85

2.3 PANS - Partially Averaged Navier-Stokes

Partially Averaged Navier-Stokes (PANS) was orginially suggested by Girimaji [6] as a bridging method between Reynolds Averaged Navier-Stokes (RANS) and Direct Numerical Solution (DNS). The reason being that it is usually not affordable to resolve all scales of motion (as DNS does), meaning that some scales has to be modeled (as RANS does). The idea is to gradually change the RANS-to-DNS ratio, i.e the modeled-to-resolved scales of motion ratio. This is done gradually in order to create a smooth transition. The parameters determining the RANS-to-DNS ration is the unresolved-to-total ratio of kinetic energy, f_k, and the unresolved-to-total ratio of dissipation, f_ε. These parameters are calculated at each point at the end of every time step to be used for the next iteration, as described by Basara et al [2]. Naturally, different choices of RANS model will result in different PANS models. The RANS model used in this study is the $\zeta - f$ model, described in section 2.2. A motivation for the use of $\zeta - f$ model can be seen in [3].
The complete PANS $\zeta - f$ model, under the assumption that $f_\varepsilon = 1$, i.e all dissipation is

modeled, is given in equations (2.3.1) to (2.3.5), note that unresolved scales are indicated by subscript u

$$\nu_u = C_\mu \zeta_u \frac{k_u^2}{\varepsilon_u} \tag{2.3.1}$$

$$\frac{Dk_u}{Dt} = (P_u - \varepsilon_u) + \frac{\partial}{\partial x_j}\left[\left(\nu + \frac{\nu_u}{\sigma_{k_u}}\right)\frac{\partial k_u}{\partial x_j}\right] \tag{2.3.2}$$

$$\frac{D\varepsilon_u}{Dt} = C_{\varepsilon 1} P_u \frac{\varepsilon_u}{k_u} - C^*_{\varepsilon 2}\frac{\varepsilon_u^2}{k_u} + \frac{\partial}{\partial x_j}\left[\left(\nu + \frac{\nu_u}{\sigma_{\varepsilon_u}}\right)\frac{\partial \varepsilon_u}{\partial x_j}\right] \tag{2.3.3}$$

$$\frac{D\zeta_u}{Dt} = f_u - \frac{\zeta_u}{k_u}P_u + \frac{\zeta_u}{k_u}\varepsilon_u\left(1 - f_k\right) + \frac{\partial}{\partial x_j}\left[\left(\nu + \frac{\nu_u}{\sigma_{\zeta_u}}\right)\frac{\partial \zeta_u}{\partial x_j}\right] \tag{2.3.4}$$

$$L^2\nabla^2 f_u - f_u = \frac{1}{T_u}\left(c_1 + C_2'\frac{P}{\varepsilon_u}\right)\left(\zeta_u - \frac{2}{3}\right) \tag{2.3.5}$$

where L and T_u is the length- and time scale respectively, P is the production term, the model coefficients $C^*_{\varepsilon 2}$ and $\sigma_{k_u,\varepsilon_u,\zeta_u}$ are

$$C^*_{\varepsilon 2} = C_{\varepsilon 1} + \frac{f_k}{f_\varepsilon}\left(C_{\varepsilon 2} - C_{\varepsilon 1}\right) \tag{2.3.6}$$

$$\sigma_{k_u,\varepsilon_u,\zeta_u} = \sigma_{k,\varepsilon,\zeta}\frac{f_k^2}{f_\varepsilon}. \tag{2.3.7}$$

f_k, the parameter that determines the unresolver-to-total kinetic energy ratio depends on the grid spacing and is defined as

$$f_k = \frac{1}{\sqrt{C_\mu}}\left(\frac{\Delta}{\Lambda}\right)^{\frac{2}{3}} \tag{2.3.8}$$

where Δ is the grid cell spacing and $\Lambda = k^{\frac{3}{2}}/\varepsilon$ is the turbulent length scale. Note, if f_k would be set to 1, the model would be identical to $\zeta - f$ RANS.
For a detailed description and derivation of the $\zeta - f$ PANS model, see Basara et al [2].

2.4 Pressure Boundaries

Pressure boundaries are commonly used when prescribing the boundary conditions for in- and outflow of an intake port. The relationship between the total pressure,p_{tot}, and the static pressure, p_b, varies depending on the direction of the flow according to

$$p_b = \begin{cases} p_{tot} - \frac{1}{2}\rho_b U_b^2 & \text{inflow} \\ p_{tot} & \text{outflow} \end{cases} \tag{2.4.1}$$

where U_b is the velocity at the boundary and ρ_b the density.

2.5 Resolution Requirements

In order to resolve enough of the turbulent structure near the wall, certain requirements on the computational grid has to be met. Namely, the size of the cells closest to the wall can not be too large. The conventional way of stating these requirements is by using n^+,

s^+ and l^+, the viscous units (or wall units). They are dimensionless quantities of the cell closest to the wall, definied as

$$n^+ = \frac{u^* n}{\nu} \tag{2.5.1}$$

$$s^+ = \frac{n^+ s}{n} \tag{2.5.2}$$

$$l^+ = \frac{n^+ l}{n} \tag{2.5.3}$$

where n is the distances normal to the wall, l the distance in the stream wise direction and s the distance in the direction that is perpendicular to both the normal and stream wise direction. $u^* = \sqrt{\tau_w/\rho}$ is the friction velocity and $\tau_w = \mu \frac{du}{dn}|_{n=0}$ is the wall shear stress. LES has rather strict resolution requirements while the requirements for PANS are a bit relaxed, they can be seen in table 2.5.1

Table 2.5.1: Resolution requirements for LES and PANS.

Unit	LES	PANS
n^+	≤ 1	≤ 1
s^+	≤ 30	≤ 100
l^+	≤ 100	≤ 200

The requirements for LES should be fulfilled in order for the turbulent scales to be fully resolved [4]. The requirements for PANS are not as well documented but rather guidelines. Besides the LES- and PANS specific requirements, there are also requirements that has to be fulfilled regardless of the solution method. The relative size difference between two neighbouring cells in the direction perpendicular to their common side should be kept below 30%. This because the solver can treat the common side as a wall if the difference exceeds 30% [12].

The Courant–Friedrichs–Lewy condition (CFL condition) is a necessary condition for convergence when solving partial differential equations by a finite difference method. The CFL condition is

$$C = \frac{u_x \Delta t}{\Delta x} + \frac{u_y \Delta t}{\Delta y} + \frac{u_z \Delta t}{\Delta z} \leq 1 \tag{2.5.4}$$

where Δx, Δy and Δz are the cell dimensions. The physical implication of this criteria is that a fluid particle is not allowed to travel through more then 1 cell during the duration of one time step. For an explicit solver this criteria must be met in all cells but most implicit solvers can converge even if some cells break the CFL condition.

Chapter 3

Method

The geometries were cleaned and organized in ANSYS ICEM CFD after which the largest part of the study took place; the creation of the computational grid, also done in ICEM. This part of the study took roughly 4 out of the total 6 months spent, mainly because of the high complexity in the geometry. Even though only half of the geometry was worked on (because of symmetry) it still needed to be divided into almost 700 blocks. When a good blocking structure was developed the iterative process between mesh generation and running simulations began. When running transient simulations such as LES and PANS the spatial resolution is important but since the friction velocity is unknown before the first simulations, the first mesh is based on a guess. The mesh needs to be tested and after that a refinement can be applied. The simulations were performed using the commercial solver AVL FIRE and they were executed on computational clusters. The results were analysed and visualized using the post processor softwares Ensight and Matlab. Figure 3.0.1 gives a visual representation of the work flow of the study.

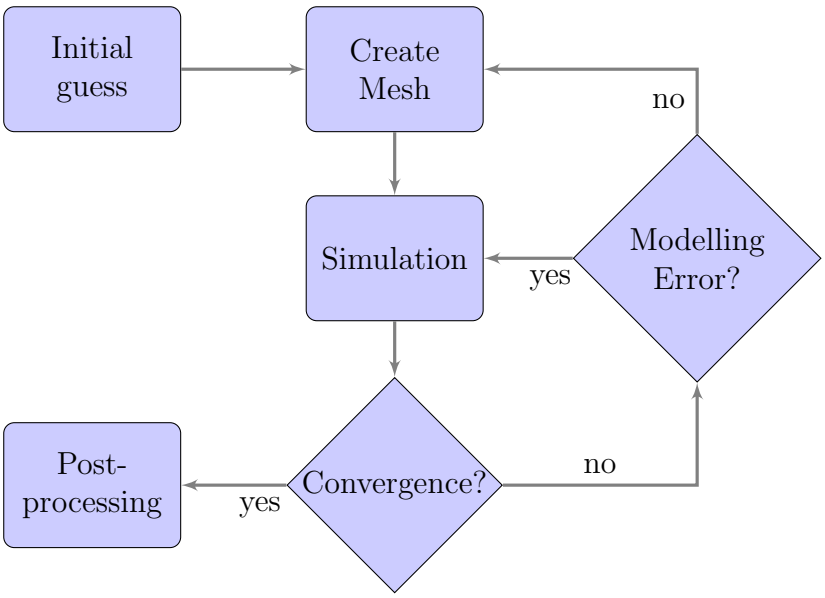

Figure 3.0.1: Work flow of the study.

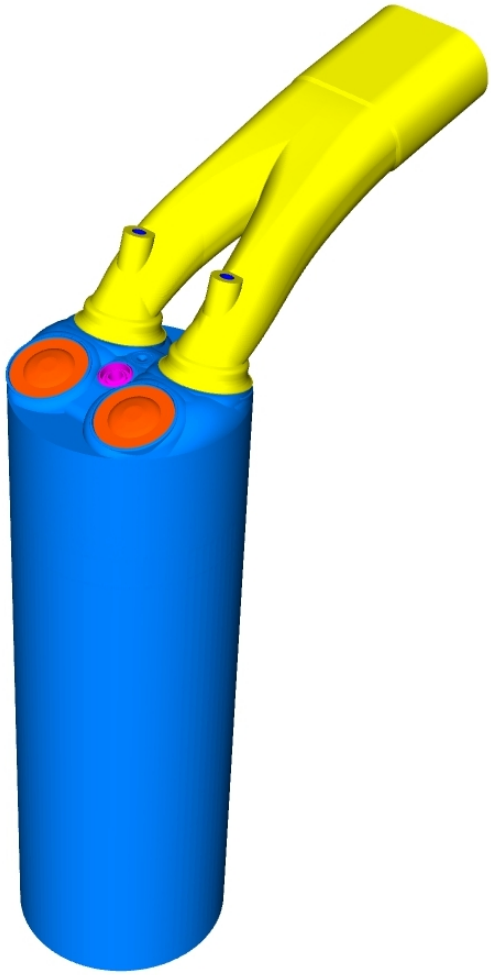

Figure 3.1.1: The entire domain.

3.1 Model Geometry

Figure 3.1.1 shows the entire computational domain. For simplicity, the domain has been divide into 3 major parts;

- the intake port (the yellow part in figure 3.1.1)
- the cylinder (the rest of the visible parts in figure 3.1.1)
- the invalve (the orange in figure 3.1.2 and 3.1.3)

The cylinder has a diameter of 84 mm and the cylinder height is 252 mm. Figure 3.1.2 shows the interior of the geometry with the invalve colored in orange while figure 3.1.3 show the geometry with the invalve lift at 6 mm and 10 mm.

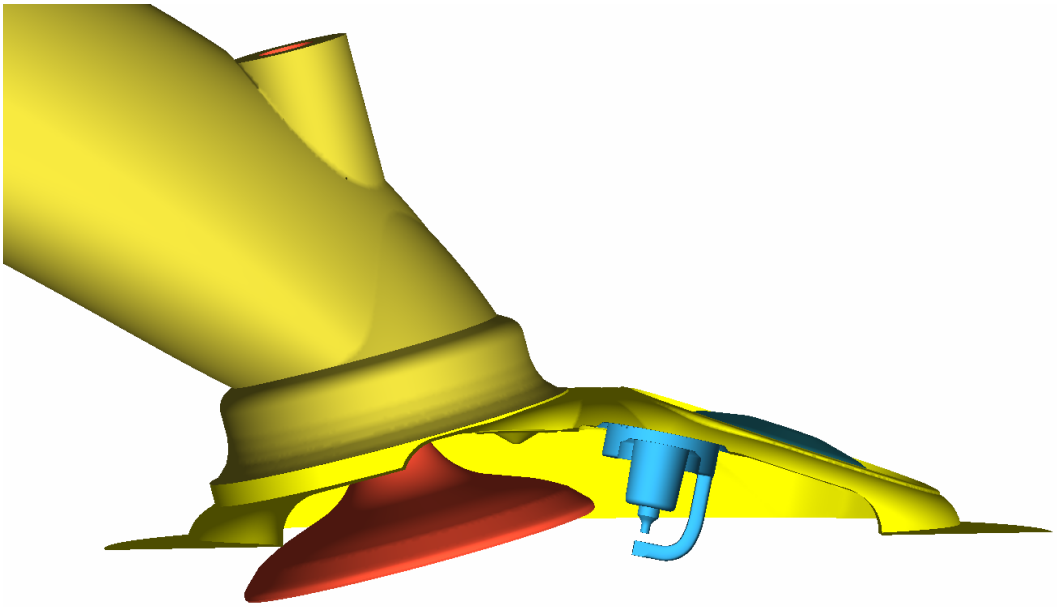

Figure 3.1.2: The interior of the domain.

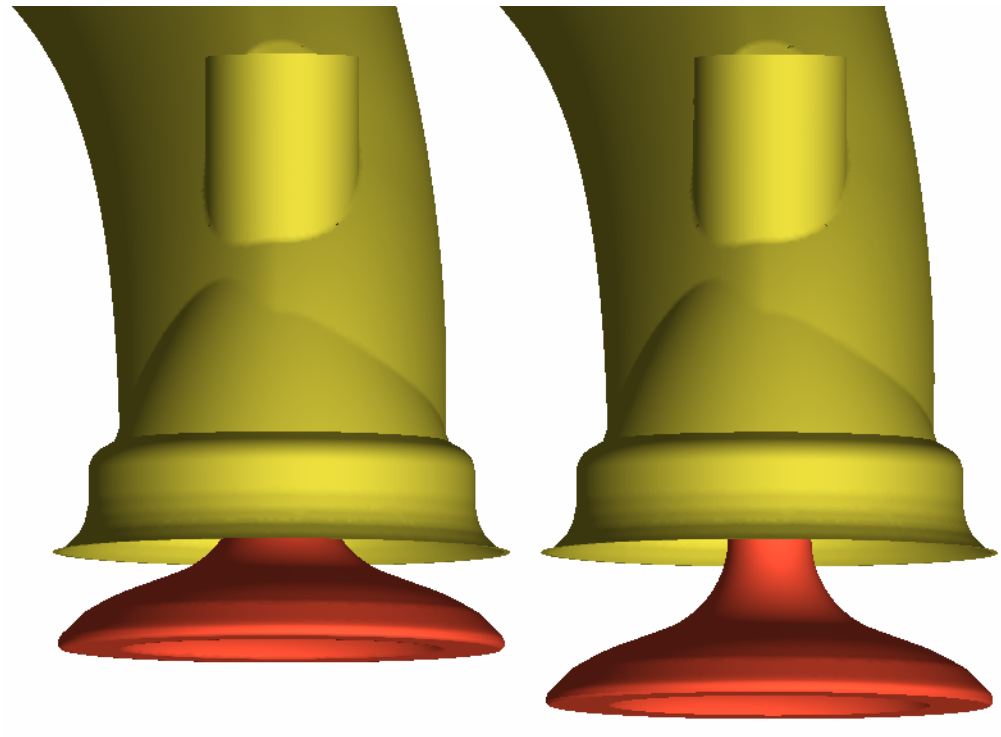

Figure 3.1.3: The invalves at 6 and 10 mm open.

3.2 The Computational Grid

The structured hexahedral computational grids (meshes) were created using ANSYS ICEM CFD. The way this is done in ICEM is called blocking where the entire geometry is divided into blocks such that the geometry is well resolved. The mesh parameters are then defined for each block i.e. number of nodes and distribution. The blocking for the geometries is shown in figure 3.2.1
How the nodes are distributed is defined by specifying the size of the cells at both ends of an edge as well specifying the percentage increase or decrease of the cell size. Since the geometry is perfectly symmetrical along the yz-plane only half of the geometry needed to be blocked. The mesh was created with the resolutions requirements for PANS in mind, see section 2.5, especially the requirement in the wall normal direction ($n^+ \leq 1$). Since the friction velocity u^* is unknown before a simulation is done and changes according to how well the flow is resolved, the mesh had to be constructed using an iterative process. First the mesh was constructed with an initial guess on how the velocity profiles would look like and then a simulation was done. Then the mesh was refined according to previous simulation results and this process continued until a satisfactory resolution was obtained. A mesh was first constructed for the case with invalve lift at 10 mm.
For the case with invalve lift at 6 mm the blocks from the 10 mm mesh were translocated around the invalve to fit the 6 mm geometry. The final meshes all consisted of 671 blocks and a total of 9.1 million cells for half of the geometry. When performing the steady state simulations (RANS) only half of the mesh was used with a symmetric boundary condition. When performing transient simulations such as PANS and LES the flow is expected to vary in time around the symmetry plane and thus, the mesh was mirrored and merged in ICEM in order to create a perfectly symmetrical mesh which then increased the mesh sizes to 18.2 million cells. The meshing process in this study took approximately 4 months out of the total 6 months spent.

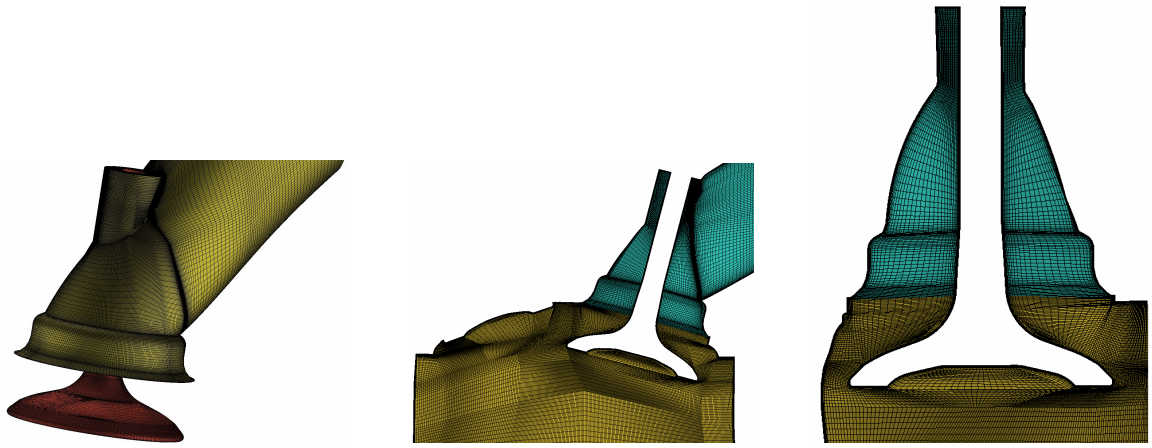

(a) The surface mesh of the intake port and the invalve

(b) A cut along the yz-plane of the mesh

(c) A cut along the xz-plane of the mesh

Figure 3.2.2: The mesh of the geometry with invalve lift at 10 mm.

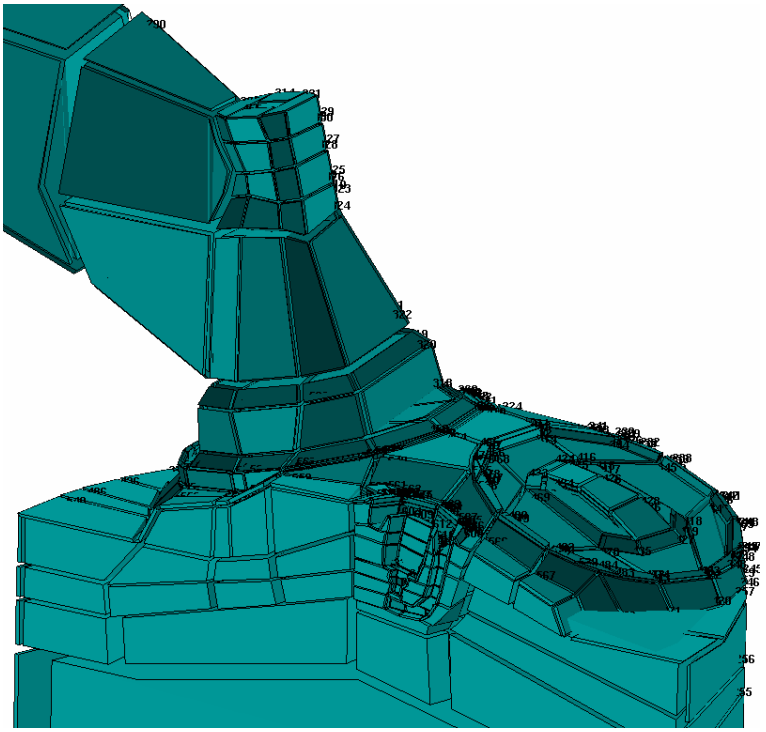

Figure 3.2.1: Blocking of the geometries.

3.3 Key Indicators

In the Benchmark report from BMW [9] the comparisons between the experiments and the two different CFD solvers (AVL FIRE and ANSYS CFX) were made with two key indicators, the isentropic flow cross-section area, A_s, and the volumetric tumble number, TU, as described in [7].

3.3.1 Isentropic Flow Cross-Section Area

The isentropic flow cross-section area is a measurement of the mass flow through the system in terms of an area and it is defined as

$$A_s = \frac{\dot{m}_{real}}{\dot{m}_{theory}} A_{ref} \tag{3.3.1.1}$$

where $\dot{m}_{real}$ is the mass flow rate at the inlet and $A_{ref} = 5542$ mm^2 the reference cross-section area, taken in the middle of the cylinder. $\dot{m}_{theory}$ is the theoretical mass flow rate for isentropic conditions, it is given as

$$\dot{m}_{theory} = A_{ref} \sqrt{\frac{2\gamma}{\gamma - 1}} \frac{p_{in}}{\sqrt{R_{gas} T_{in}}} \sqrt{\left(\frac{p_{cyl}}{p_{in}}\right)^{2/\gamma} - \left(\frac{p_{cyl}}{p_{in}}\right)^{(\gamma+1)/\gamma}} \tag{3.3.1.2}$$

where

- $\gamma = 1.4$ is the heat capacity ratio for air,
- R_{gas} is the gas constant of air,
- p_{in} is the total pressure at the inlet,

- p_{cyl} is the average pressure in the cylinder,
- T_{in} is the temperature at the inlet.

3.3.2 Volumetric Tumble Number

The volumetric tumble number is a measurement of the tumble in the cylinder, see figure 3.3.2.1 for a visual explanation of tumble. The total volumetric tumble number is calculated by averaging the tumble number for five planes in the cylinder. These five planes are parallel to the xy-plane and are located as specified in table 3.3.2.1. Figure 3.3.2.2 gives a geometric view of where the planes are located.

Table 3.3.2.1: The position of the tumble planes.

z-location of tumble planes				
−32 mm	−37 mm	−42 mm	−47 mm	−52 mm

The tumble number for plane n is calculated as

$$TU_n = \frac{-D}{\rho_{out}\dot{V}^2} M_{x,n} \tag{3.3.2.1}$$

where ρ_{out} is the area averaged static density at the outlet, $D = 84$ mm is the bore diameter, $\dot{V}$ the volumetric flow rate at the outlet. $M_{x,n}$ is the torque around the x-axis of plane n, calculated as

$$M_{x,n} = \sum_i \rho_i A_{i,n} Y_i w_i |w_i| \tag{3.3.2.2}$$

where ρ_i is the static density at face area i, $A_{i,n}$ is the area of face i of plane n, Y_i is the y-coordinate of center of face i and w_i is the velocity component in the z-direction at the center of face i [7].

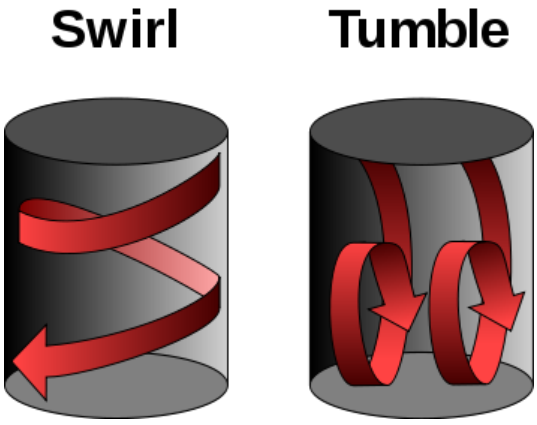

Figure 3.3.2.1: Swirl and Tumble [1]

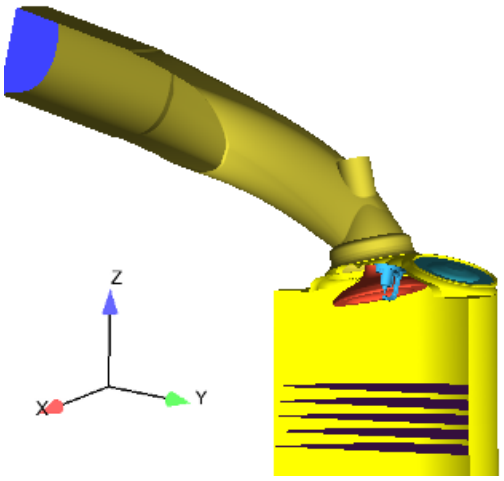

Figure 3.3.2.2: The location of the tumble planes. The bore diameter, D, is the same as the diameter of the outlet.

3.4 BMW Benchmark

A benchmark study was performed by BMW with 4 different CFD codes together with the experimental data. The goal of the benchmark was to measure the same key indicators as the experiment, namely the isentropic cross-section area and the volumetric tumble number. It is however only the result from the FIRE and CFX simulations that can be made public. The experiments was averaged over 5 cylinder heads with 6 cylinders each [9]. The results of the simulations and experiments along with the standard deviations, σ, can be seen in table 3.4.0.1 and 3.4.0.2. As can be seen in this tables the simulations predict the isentropic cross-section area fairly close to the measured experiments but the predictions of the volumetric tumble number match poorly with the experiments.

Table 3.4.0.1: The isentropic cross-section area, A_s [mm^2], from the benchmark.

Valve lift	Experiment	σ_{A_s} [%]	FIRE	CFX
6 mm	620.67	2.57	604	620
10 mm	683.87	2.52	652	680

Table 3.4.0.2: The volumetric tumble number, TU [-], from the benchmark.

Valve lift	Experiment	σ_{TU} [%]	FIRE	CFX
6 mm	2.51	7.64	0.995	0.82
10 mm	3.13	4.88	1.592	1.02

3.5 Numerical Method

The equations for LES and PANS (see Chapter 2) are discretized both in time and space, RANS is a steady state solution method and it is thus not discretized in time. The flow is

then solved with the three different models on the two meshes described in section 3.2. The algorithm Semi-Implicit Method for Pressure Linked Equations (SIMPLE) is used for all three models. SIMPLE is a commonly used numerical procedure to solve the Navier-Stokes equations. The flow is modeled as incompressible, a choice made based on the results from the RANS simulation performed by AVL FIRE for the benchmark and discussions with Dr. Branislav Basara at AVL List GmbH. The CFD solver used in this study was AVL Fire.

3.5.1 Boundary Conditions

The boundary conditions for the simulations are given in table 3.5.1.1

Table 3.5.1.1: The boundary conditions for the simulations.

Fluid	Air
Inlet	Total pressure of 1 bar Temperature of 293.15 K
Outlet	Averaged static pressure of 0.9 bar
Walls	Velocity = 0 Temperature of 293.15 K

3.5.2 LES Settings in AVL FIRE

The settings for the simulation is showed in table 3.5.2.1, where URF stands for under-relaxation factor.

Table 3.5.2.1: The solver settings for LES.

Settings for LES	
Time step	6×10^{-7}s
URF momentum	0.3
URF pressure	0.3
Differencing Scheme momentum	95% Central Differencing 5% Upwind
Differencing Scheme pressure	100% Central Differencing

3.5.3 PANS Settings in AVL FIRE

Table 3.5.3.1: The solver settings for PANS.

Settings for PANS	
Time step	6 $\times 10^{-7}$s
URF momentum	0.4
URF pressure	0.4
URF kinetic energy	0.35
URF dissipation	0.35
Differencing Scheme momentum	100% MINMOD Relaxed
Differencing Scheme pressure	100% Central Differencing

MINMOD is a second order upwind scheme with improved convergence but with slightly decreased accuracy.
Aside from these settings, the PANS model requires that the turbulent kinetic energy k is defined at the inlet. An appropriate way of doing this is to base the esimation on experimental data or set low so that the flow going into the domain is laminar and then further into the domain become turbulent.
The turbulent kinetic energy k is in this study estimated by defining a turbulence intensity I defined as

$$I = \frac{u'}{U} = \frac{(2/3k)^{1/2}}{U} \tag{3.5.3.1}$$

where u' is the averaged r.m.s velocity and U is the mean flow velocity.

3.5.4 RANS Settings in AVL FIRE

Table 3.5.4.1: The solver settings for RANS.

Settings for RANS	
URF momentum	0.4
URF pressure	0.05
URF kinetic energy	0.2
URF dissipation	0.2
Differencing Scheme momentum	100% MINMOD Bounded
Differencing Scheme pressure	100% Central Differencing

3.5.5 Averaging Results

The flow properties from the transient simulations (LES and PANS) has to be time averaged in order for the result to be accurate. The time averaging began when two criterias were fulfilled

- A particle had traveled through the geometry once
- The two key indicators had stabilized

3.6 Computational Resources

Since the meshes were large, the calculations were performed using MPI on 192 processor cores. The simulations were run on both the National Supercomputer Centre (NSC) at Linköping University, Sweden and the Centre for Scientific and Technical Computing (C3se) at Chalmers University of Technology, Sweden. The wall clock time for a simulation using 192 processor cores was roughly 10 days.

Chapter 4

Results

In this chapter the results of the RANS, PANS and LES simulations are presented and compared. First, the spatial resolution for the different models is presented illustrating how well the different mathematical models predict the fluid flow near the surfaces. The streamlines from the averaged flows are compared and two vortices are identified to be of major importance for the volumetric tumble number. The key indicators isentropic cross-section area and volumetric tumble number are presented for each simulation model and valve lift case. Thereafter the impact of the different inlet conditions of the turbulent intensities for PANS are showed and compared. Lastly, a comparison between the PANS and LES results in terms of the turbulent kinetic energy resolved, unresolved and resolved-to-total ratio are looked upon.

4.1 Resolution

The spatial resolutions for the different models is calculated in terms of viscous units as described in section 2.5. The same mesh is used for each valve lift case implying that the differences in viscous units comes from how the mathematical models predict the flow.

4.1.1 The CFL number

In terms of the CFL number the spatial resolution was well within reasonable values, see table 4.1.1.1, implying that the time step of 6×10^{-7}s was small enough.

Table 4.1.1.1: Resolution in terms of the CFL number for the LES simulation.

	LES		**PANS**	
	6 mm	10 mm	6 mm	10 mm
Max	5.27	6.33	5.30	5.83
Mean	0.035	0.038	0.036	0.040

4.1.2 LES

The spatial resolution for the LES simulations of both the 6 mm and 10 mm mesh in terms of wall units is summarized in table 4.1.2.1 and visualized in figure 4.1.2.1.

Table 4.1.2.1: Spatial resolution in terms of wall units for the LES simulations.

LES		**6 mm**			**10 mm**		
		n^+	s^+	l^+	n^+	s^+	l^+
Invalve	Max	2.05	205	205	2.23	223	223
	Mean	0.54	54	54	0.62	62	52
Intake Port	Max	5.81	76	175	10.15	132	305
	Mean	0.52	52	173	0.61	61	203
Cylinder	Max	6.23	623	1350	2.99	299	650
	Mean	0.27	27	180	0.27	27	180

The spatial resolution in the normal direction of the surface is fulfilled in the domain except in a few cells. However, in the span wise and lengthwise directions, the resolution requirements are not met.

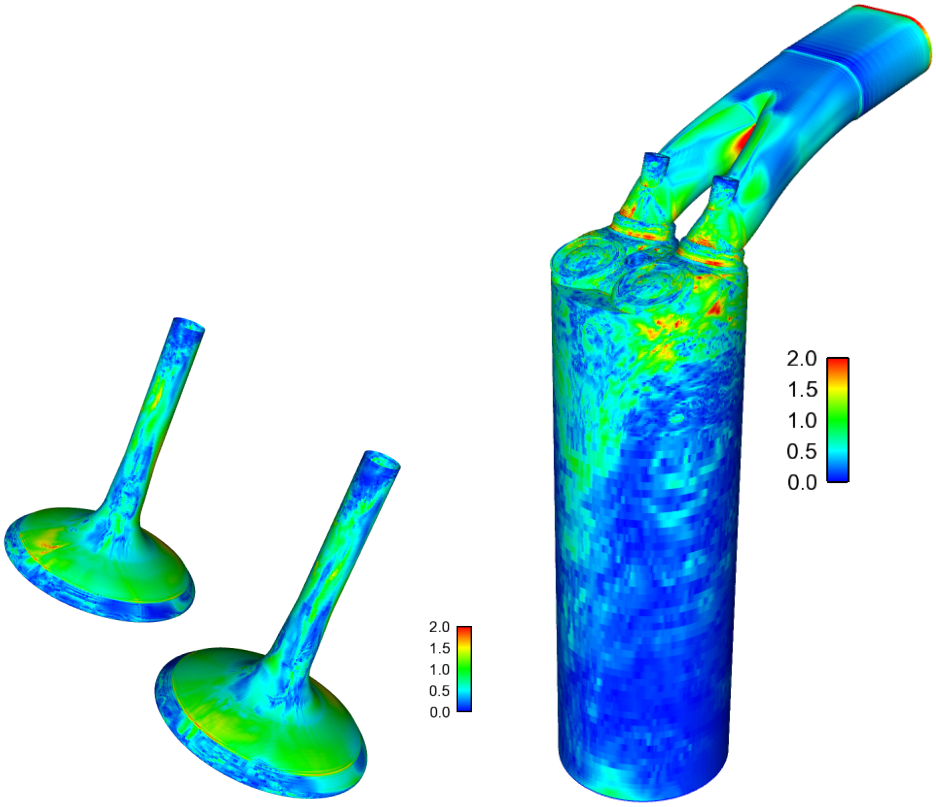

(a) Invalve 6 mm

(b) Entire domain 6 mm

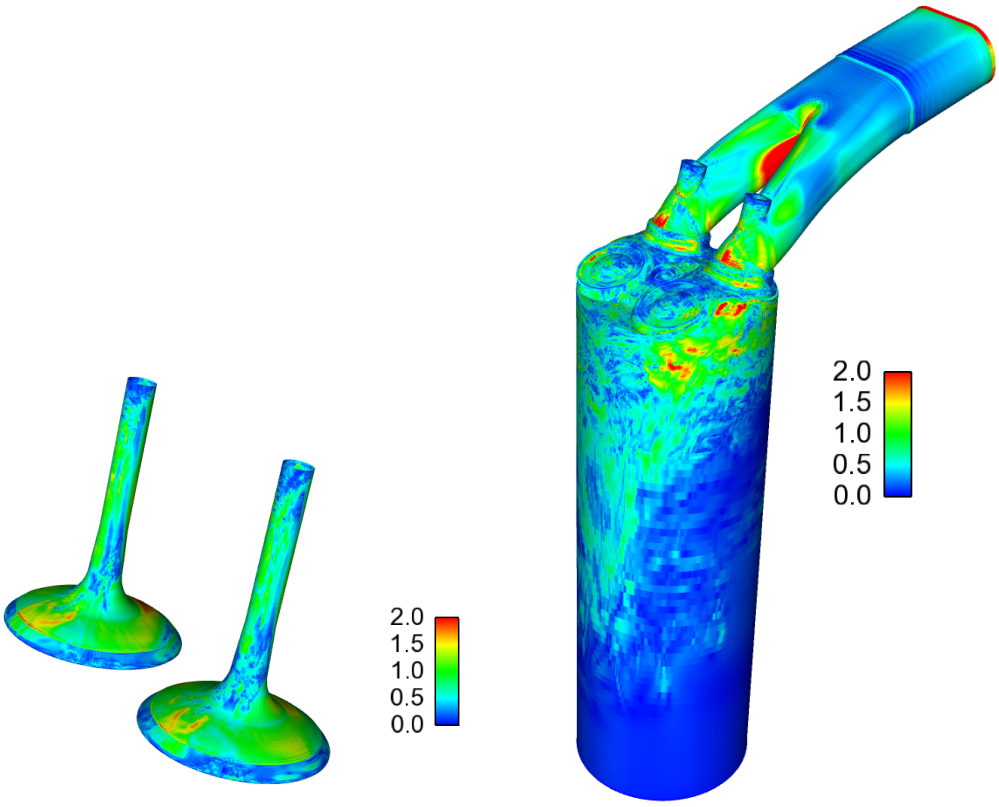

(c) Invalve 10 mm

(d) Entire domain 10 mm

Figure 4.1.2.1: LES: n^+ values of 6 mm (top) and 10 mm (bottom).

4.1.3 PANS

The spatial resolution for the PANS simulations of both the 6 mm and 10 mm mesh in terms of wall units is summarized in table 4.1.3.1 and visualized in figure 4.1.3.1. As can be seen in table 4.1.3.1, the mesh should be well suited for PANS, see section 4.1.

Table 4.1.3.1: Spatial resolution in terms of wall units for the PANS simulation.

PANS		**6 mm**			**10 mm**		
		n^+	s^+	l^+	n^+	s^+	l^+
Invalve	Max	2.73	491	664	2.74	493	667
	Mean	0.41	39	100	0.37	35	90
Intake Port	Max	5.02	140	502	5.9	165	590
	Mean	0.35	33	175	0.30	28	150
Cylinder	Max	4.01	469	802	1.90	222	380
	Mean	0.21	25	140	0.16	19	107

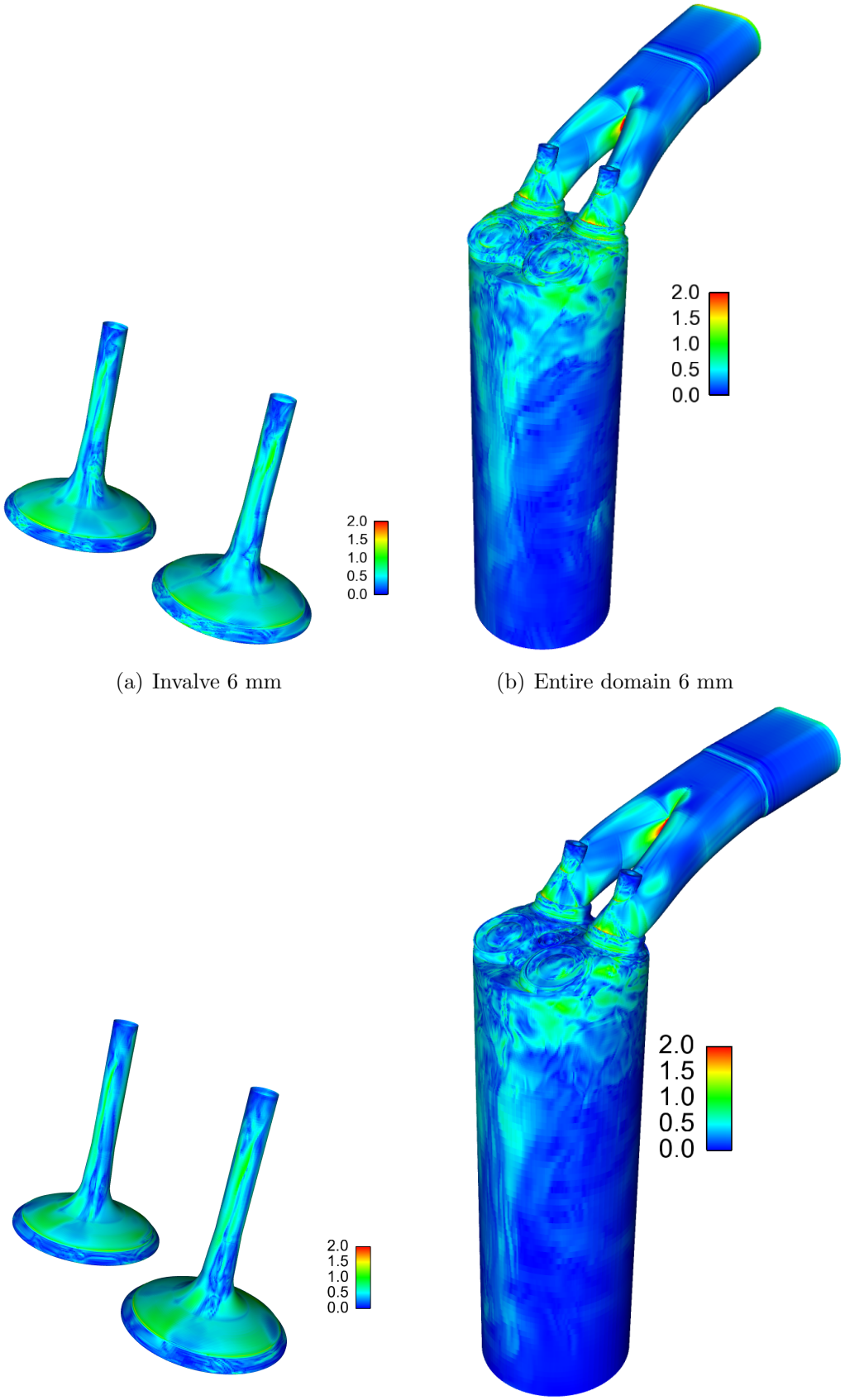

(a) Invalve 6 mm

(b) Entire domain 6 mm

(c) Invalve 10 mm

(d) Entire domain 10 mm

Figure 4.1.3.1: PANS: n^+ values of 6 mm (top) and 10 mm (bottom).

4.1.4 RANS

The spatial resolution for the RANS simulations of both the 6 mm and 10 mm mesh in terms of wall units is summarized in table 4.1.4.1 and visualized in figure 4.1.4.1.

Table 4.1.4.1: Spatial resolution in terms of wall units for the RANS simulation.

RANS		**6 mm**			**10 mm**		
		n^+	s^+	l^+	n^+	s^+	l^+
Invalve	Max	1.44	163	67	1.39	139	93
	Mean	0.0080	8	6.7	0.10	10	8
Intake Port	Max	3.92	51	118	5.64	73	169
	Mean	0.056	5.6	19	0.07	7	23
Cylinder	Max	1.14	133	38	0.68	215	136
	Mean	0.055	5.5	37	0.05	5	33

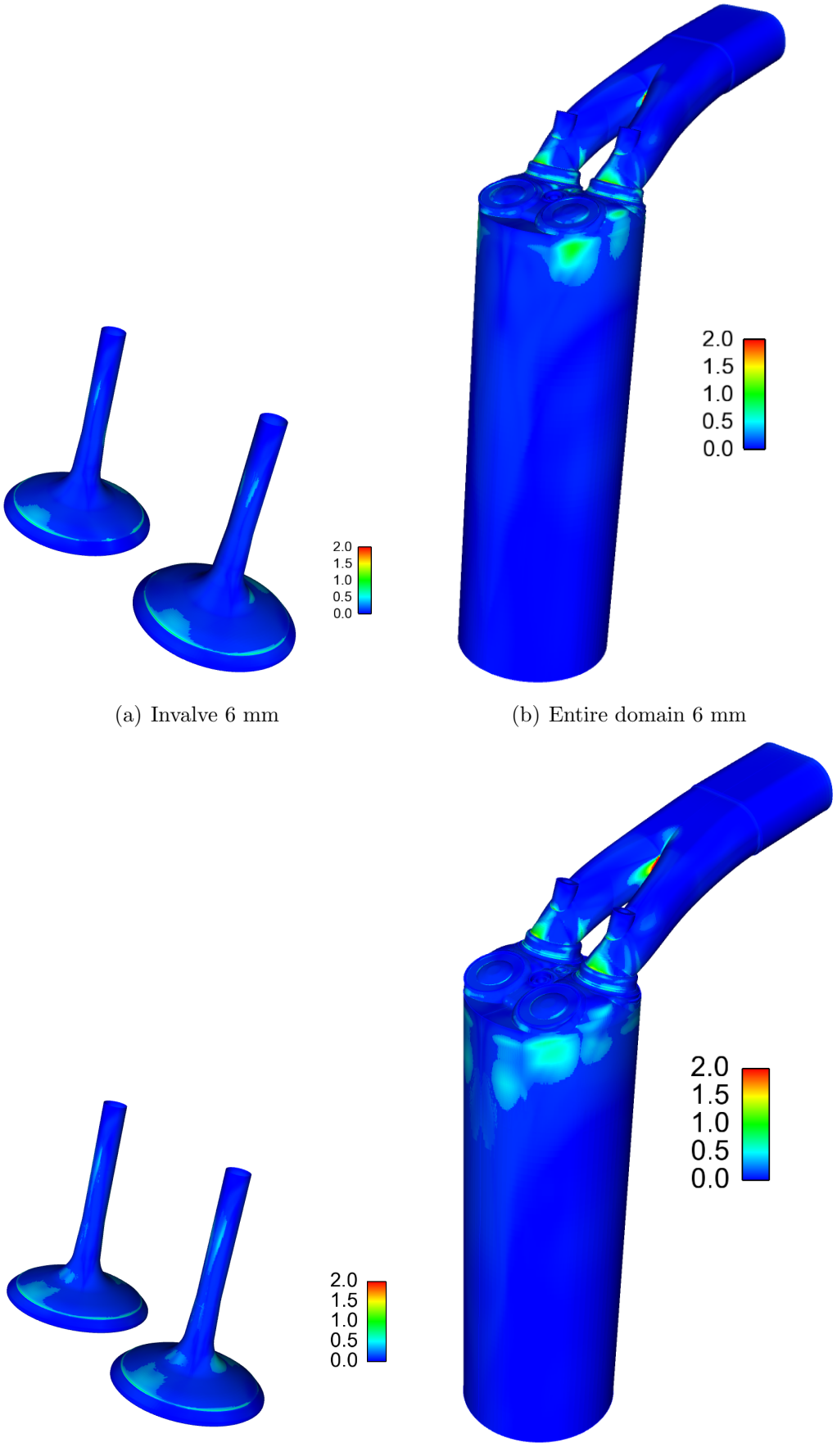

(a) Invalve 6 mm

(b) Entire domain 6 mm

(c) Invalve 10 mm

(d) Entire domain 10 mm

Figure 4.1.4.1: RANS: n^+ values of 6 mm (top) and 10 mm (bottom).

4.2 Flow Visualizations

How the air flows in the cylinder is visualized by the streamlines created from the RANS, PANS and LES results. Figure 4.2.1 and 4.2.2 shows the streamlines in a yz-plane at the center of the invalve. Two vortex structures can here be identified in all simulations as large influences in the value of the volumetric tumble number. Both are located under the invalve where the left vortex core rotates in a counter clockwise direction and the right vortex core rotates in a clockwise direction. As seen in equation (3.3.2.1) the volumetric tumble number is dependent on the torque around the x-axis. The left vortex structure has high velocities going down into the cylinder and will give a negative contribution to the torque around the x-axis. The right vortex structure will because of its opposite direction and also high velocities going down into the cylinder give a positive contribution to the torque around the x-axis. Since the volumetric tumble number is defined with a minus sign the left vortex core will increases and the right vortex core will decrease the volumetric tumble number.

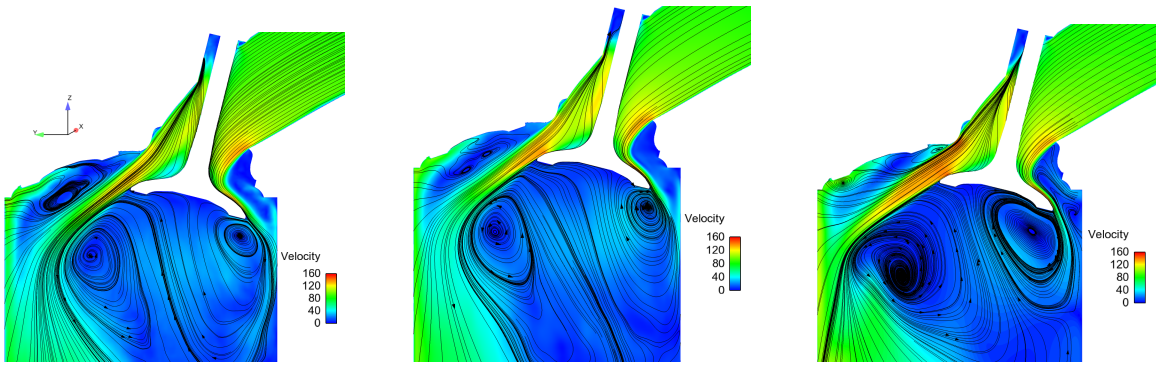

(a) LES (b) PANS (c) RANS

Figure 4.2.1: Streamlines at $x = 20$ mm, i.e. through the center of the invalve, for 10 mm invalve lift.

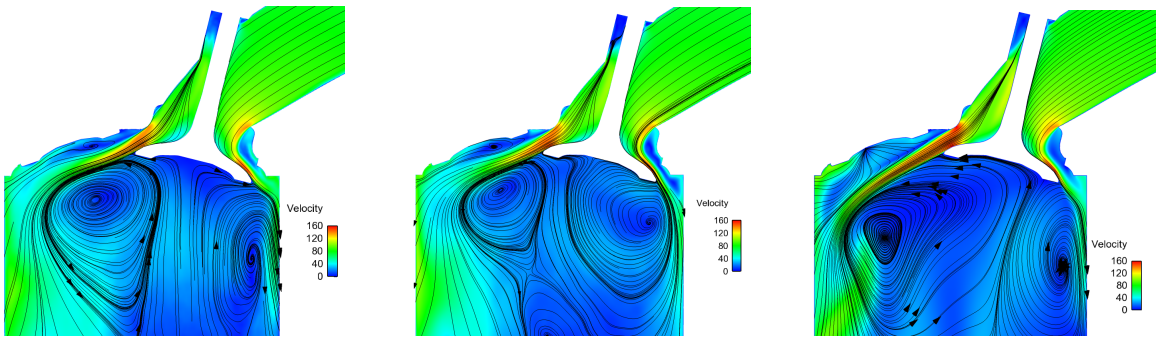

(a) LES (b) PANS (c) RANS

Figure 4.2.2: Streamlines at $x = 20$ mm, i.e. through the center of the invalve, for 6 mm invalve lift.

Figures 4.2.3 and 4.2.4 shows vortex core extractions and streamlines projected onto several planes.

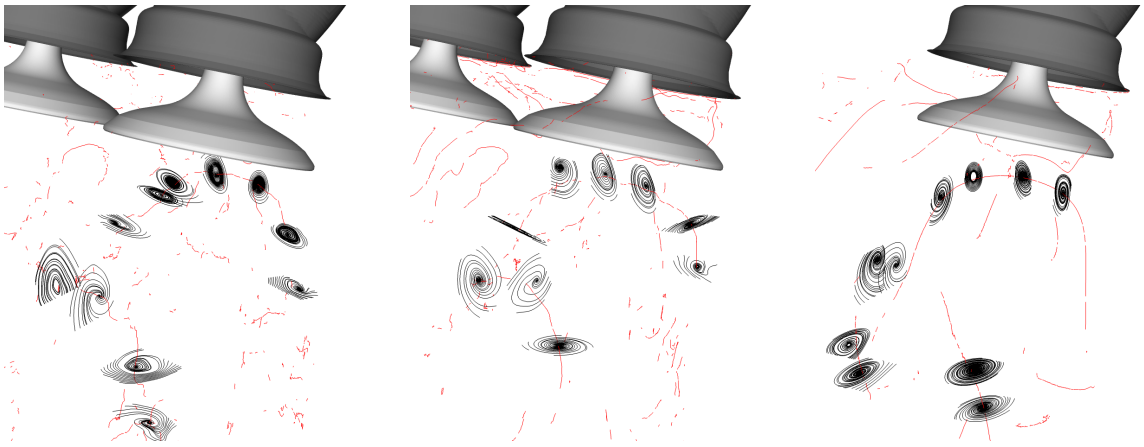

(a) LES (b) PANS (c) RANS

Figure 4.2.3: Vortex cores and streamlines at projected planes for 10 mm invalve lift.

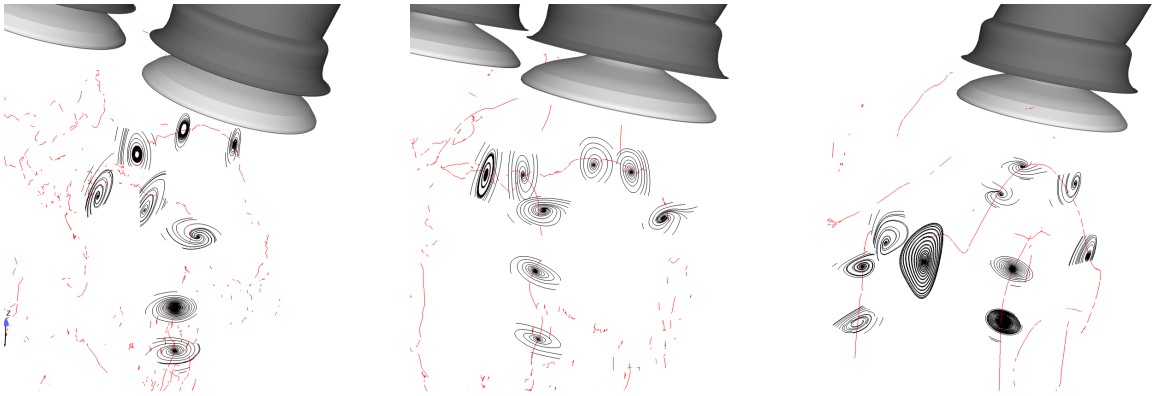

(a) LES (b) PANS (c) RANS

Figure 4.2.4: Vortex cores and streamlines at projected planes for 6 mm invalve lift.

4.3 Key Indicators

When the flow was fully developed, the result in terms of the key indicators was averaged in order to make the result from the simulations comparable to the experimental data.

4.3.1 Isentropic Cross-Section Area

The isentropic cross-section area was calculated according to equation (3.3.1.1) for each of the three solution methods; LES, PANS and RANS. The result of the simulations can be seen in table 4.3.1.1 and it is visualized in figure 4.3.1.1.

Table 4.3.1.1: Isentropic cross-section area, A_s, for experiment, LES, PANS and RANS.

Valve lift	Experiment	LES	PANS	RANS
6 mm	620.67	631	644	669
10 mm	683.87	705	708	718

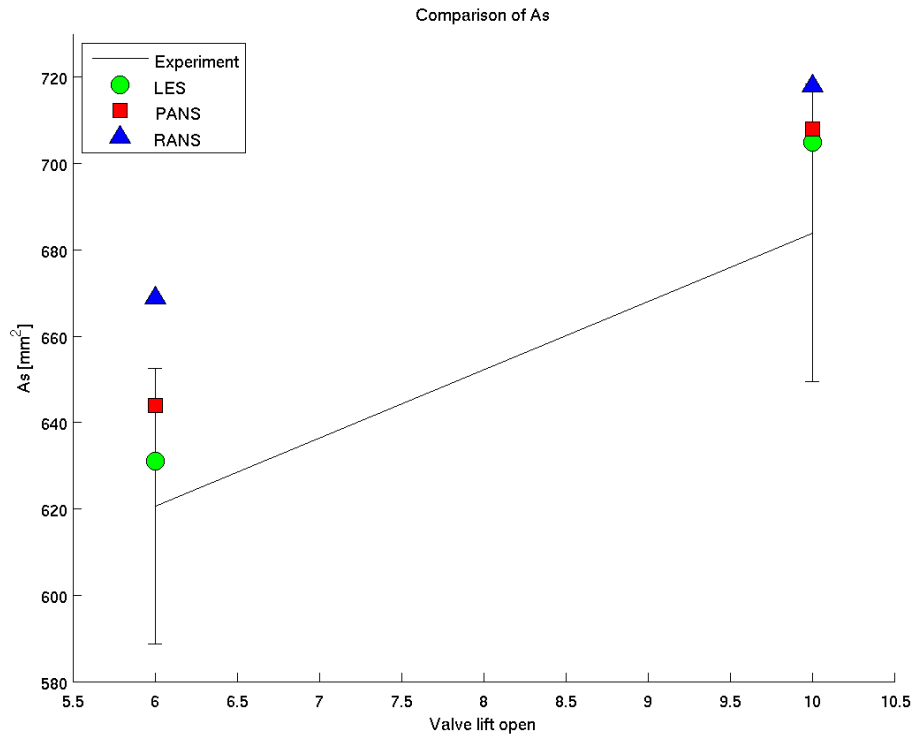

Figure 4.3.1.1: The isentropic cross-section area for the simulations and the experiment with two standard deviations.

The isentropic cross-section area from the simulations are in good agreement with the experiment, below 4% discrepancy for LES and PANS and below 8% discrepancy for RANS, see table 4.3.1.2.

Table 4.3.1.2: Percentage, [%], difference of the isentropic cross-section area from experiment.

Valve lift	LES	PANS	RANS
6 mm	1.66	3.76	7.79
10 mm	3.09	3.53	4.99

4.3.2 Volumetric Tumble Number

The volumetric tumble number was calculated as in section 3.3.2 for each of the three solution methods; LES, PANS and RANS. The result of the simulations along with the experimental data can be seen in table 4.3.2.1 and it is visualized in figure 4.3.2.1.

Table 4.3.2.1: Volumetric tumble number, TU, for experiment, LES, RANS and PANS.

Valve lift	Experiment	LES	PANS	RANS
6 mm	2.51	1.01	1.06	1.19
10 mm	3.13	1.50	1.59	1.62

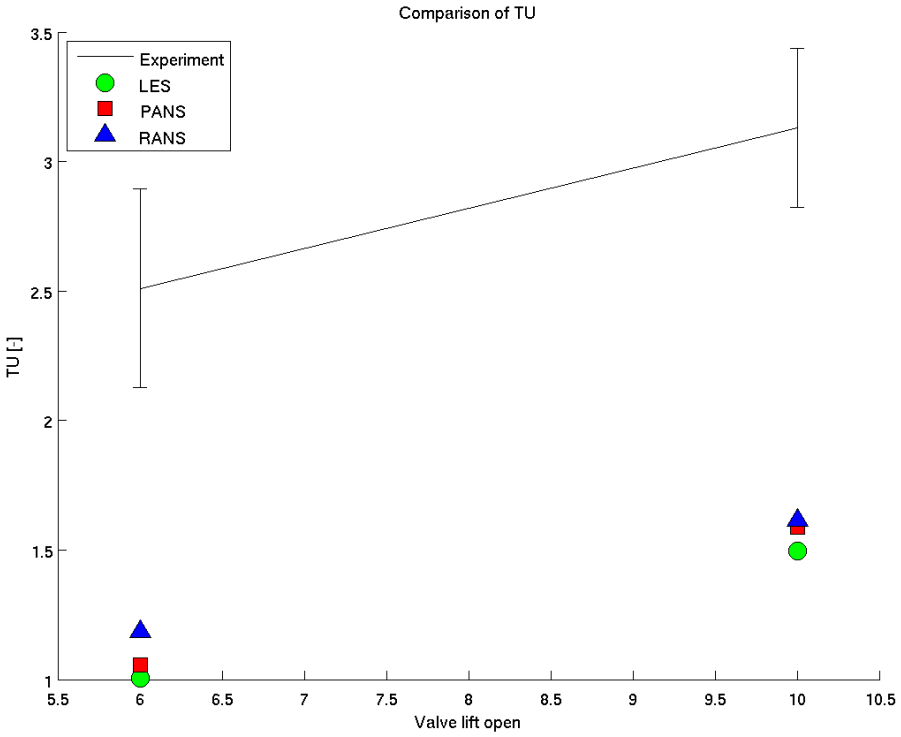

Figure 4.3.2.1: The volumetric tumble number for the simulations and the experiment with two standard deviations.

The volumetric tumble number does not agree very well with the experimental data. The simulations underestimate the volumetric tumble number by 48% - 60% as can be seen from table 4.3.2.2.
Due to the fact that the experiments are confidential, no conclusions can be made regarding the large discrepancies in the volumetric tumble number.

Table 4.3.2.2: Percentage, [%], difference of the volumetric tumble number from experiment.

Valve lift	LES	PANS	RANS
6 mm	59.9	57.9	52.8
10 mm	52.2	49.2	48.4

4.4 PANS Settings

As mentioned in section 3.5.3, the inlet conditions in terms of the turbulent kinetic energy has to be specified when running the PANS simulations. The best way of estimating the turbulent kinetic energy on the inlet would be to use experimental data. However there are no experimental data of this sort available, therefore 3 different estimations of the turbulent kinetic energy were done. Because of the similarities of the geometries, the investigation was only made with the invalve lift at 6 mm. Table 4.4.1 shows the three different cases by the turbulent intensity, I, as defined in equation (3.5.3.1).

Table 4.4.1: Cases (a), (b) and (c) in terms of their respective turbulent intensity, I.

I	[%]
(a)	1
(b)	0.09
(c)	0.0002

Figure 4.4.1 shows the total turbulent kinetic energy of the three different inlet settings for PANS together with the LES results. The impact of the inlet settings is further visualized in figure 4.4.1.3, where f_k, the computed unresolved-to-total ratio of the turbulent kinetic energy is shown. f_k is calculated as

$$f_k = \frac{<k_u>}{<k_u> + <k_r>} \tag{4.4.1}$$

where k_u is the unresolved turbulent kinetic energy and k_r is the resolved turbulent kinetic energy. k_u is computed from the transport equations for PANS and it is computed from the Smagorinsky model for LES as $k_u = k_{sgs} = C_s^2|S|^2/\nu_{sgs}$. The resolved turbulent kinetic energy is defined as $k_r = 0.5(\overline{u^2} + \overline{v^2} + \overline{w^2})$ where u, v, and w are computed fluctuations from the time-averaged velocity components and "-" indicates time-averaging.
Figure 4.4.2 clearly shows the impact that the inlet conditions has on the unresolved-to-total ratio of turbulent kinetic energy. For example, in case (c) a high unresolved-to-total ratio of turbulent kinetic energy was obtained meaning that the model uses much RANS for the simulations. Since an estimation of the experimental turbulence intensity does not exist the most physical case is unknown. The general flow structures are however similar in all three cases and thus, the key indicators are unchanged as well. However, seperation lines and more detailed flow structures are most likely different. Due to the limited time frame of this study only one case was further analyzed together with the LES results, case (b).

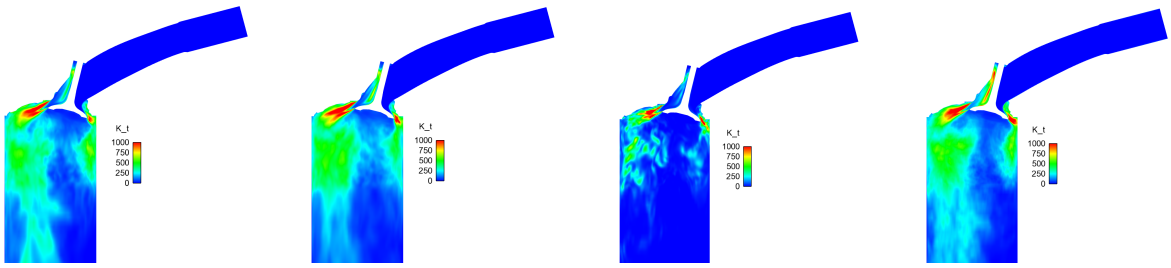

(a) PANS $I = 0.0002\%$ (b) PANS $I = 0.09\%$ (c) PANS $I = 1\%$ (d) LES

Figure 4.4.1: 6 mm: comparison of the total turbulent kinetic energy for LES and PANS with three different inlet settings.

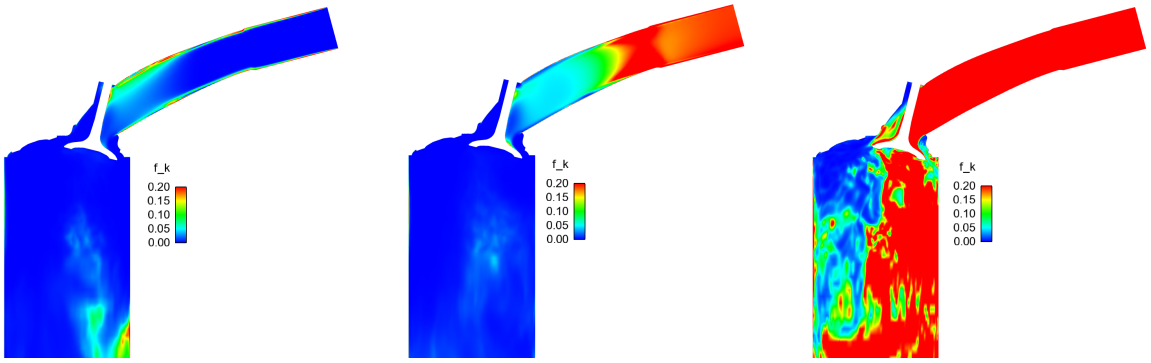

(a) PANS $I = 0.0002\%$ (b) PANS $I = 0.09\%$ (c) PANS $I = 1\%$

Figure 4.4.2: 6 mm: comparison of f_k, the unresolved-to-total ratio of turbulent kinetic energy for PANS with three different inlet settings.

4.4.1 PANS vs LES in terms of Resolved and Unresolved Turbulent Kinetic Energy

To further compare the PANS and LES results the turbulent kinetic energy resolved, unresolved and resolved-to-total ratio are looked upon. Figure 4.4.1.1 shows a comparison of the resolved turbulent kinetic energy between LES and PANS for both 10 and 6 mm. It can be seen that LES resolves more turbulent flow structures than PANS. The 6 mm case has lower velocities and therefore the resolved turbulent kinetic energy is lower than for the 10 mm case.
Figure 4.4.1.2 compares the unresolved turbulent kinetic energy between LES and PANS for both 10 and 6 mm. It can be seen that the modeling of the turbulent kinetic energy is very different between the two models. An expected result of this comparision would be as in the study by Krajnović et al. [11] where PANS has higher unresolved turbulent kinetic energy than LES. That is however not the case in this study, but instead the opposite. This phenomena could be due to the fact that the mesh resolution requirements are not met for the LES simulations. Another possible explanation is the uncertainty regarding the inlet conditions. By looking at the equations for LES and PANS it is expected that PANS would model more turbulent kinetic energy than LES. Figure 4.4.1.3 shows a comparison of the averaged unresolved-to-total ratio of turbulent kinetic energy between LES and PANS for both 10 and 6 mm. Similarly to figure 4.4.1.2 this shows the opposite of what would be expected. Again, the two possible explanations mentioned earlier could be the reasons for these results.

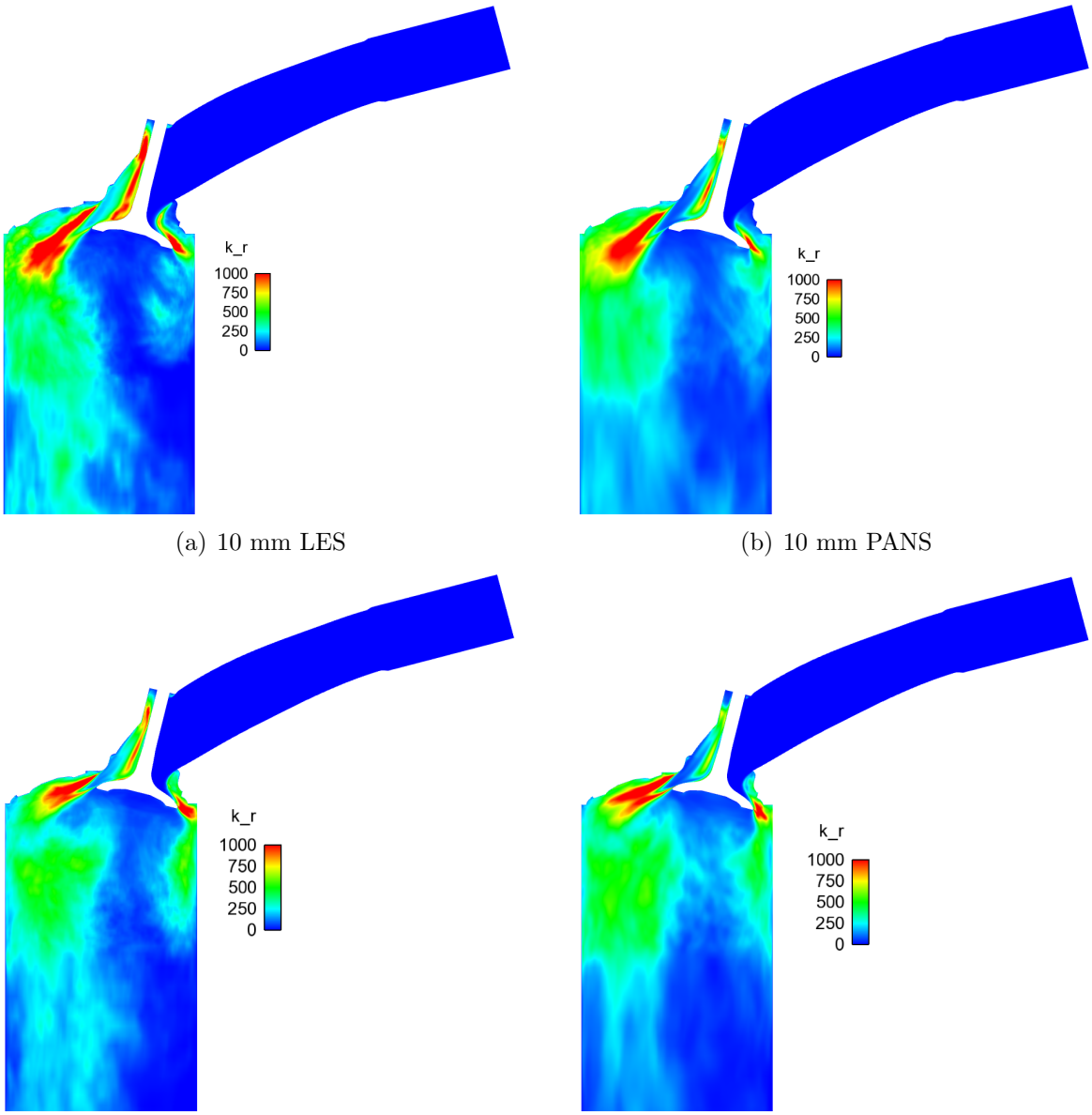

(a) 10 mm LES

(b) 10 mm PANS

(c) 6 mm LES

(d) 6 mm PANS

Figure 4.4.1.1: Comparison of the averaged resolved turbulent kinetic energy between LES and PANS for both 10 and 6 mm.

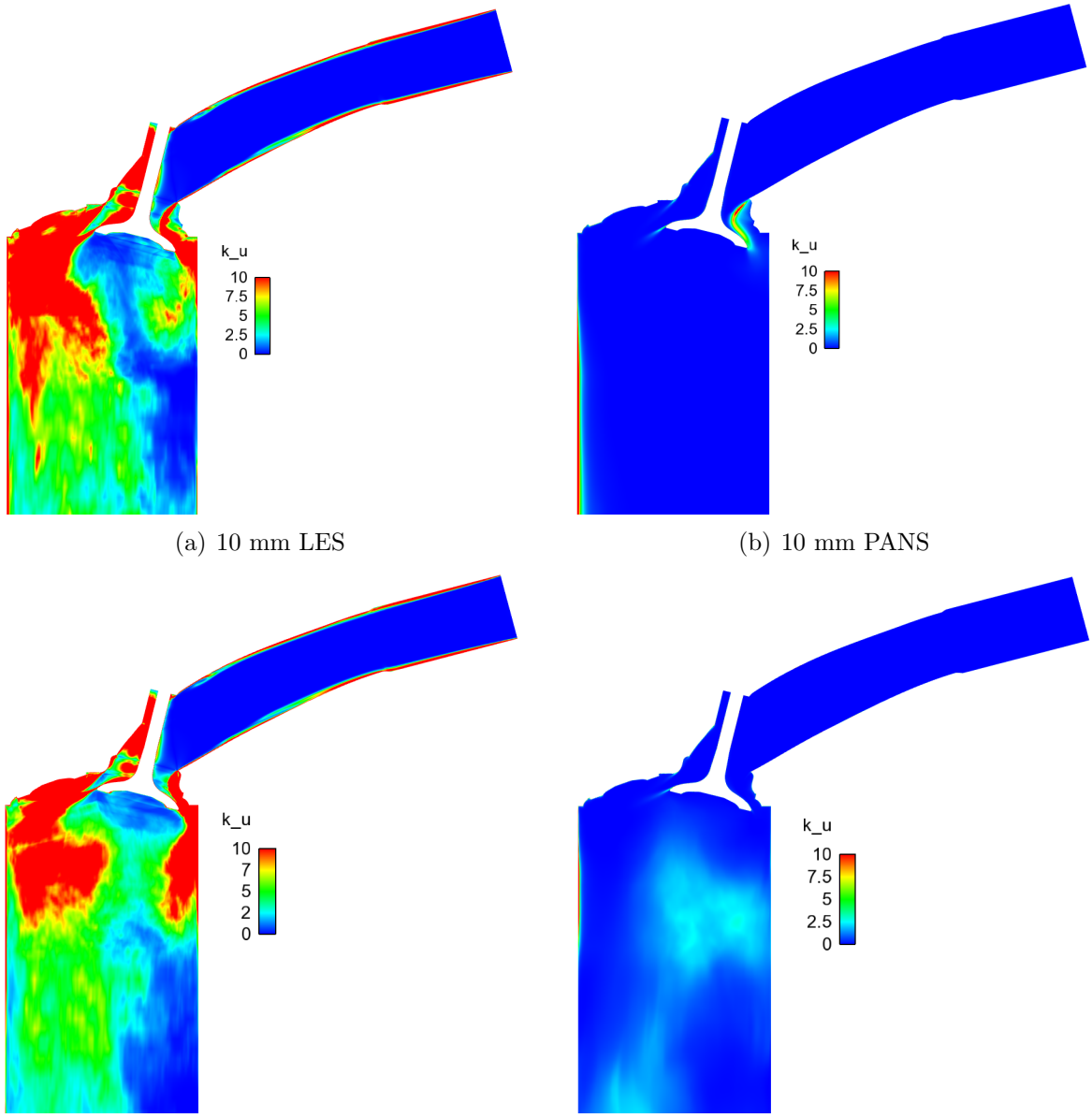

(a) 10 mm LES

(b) 10 mm PANS

(c) 6 mm LES

(d) 6 mm PANS

Figure 4.4.1.2: Comparison of the averaged unresolved turbulent kinetic energy between LES and PANS for both 10 and 6 mm.

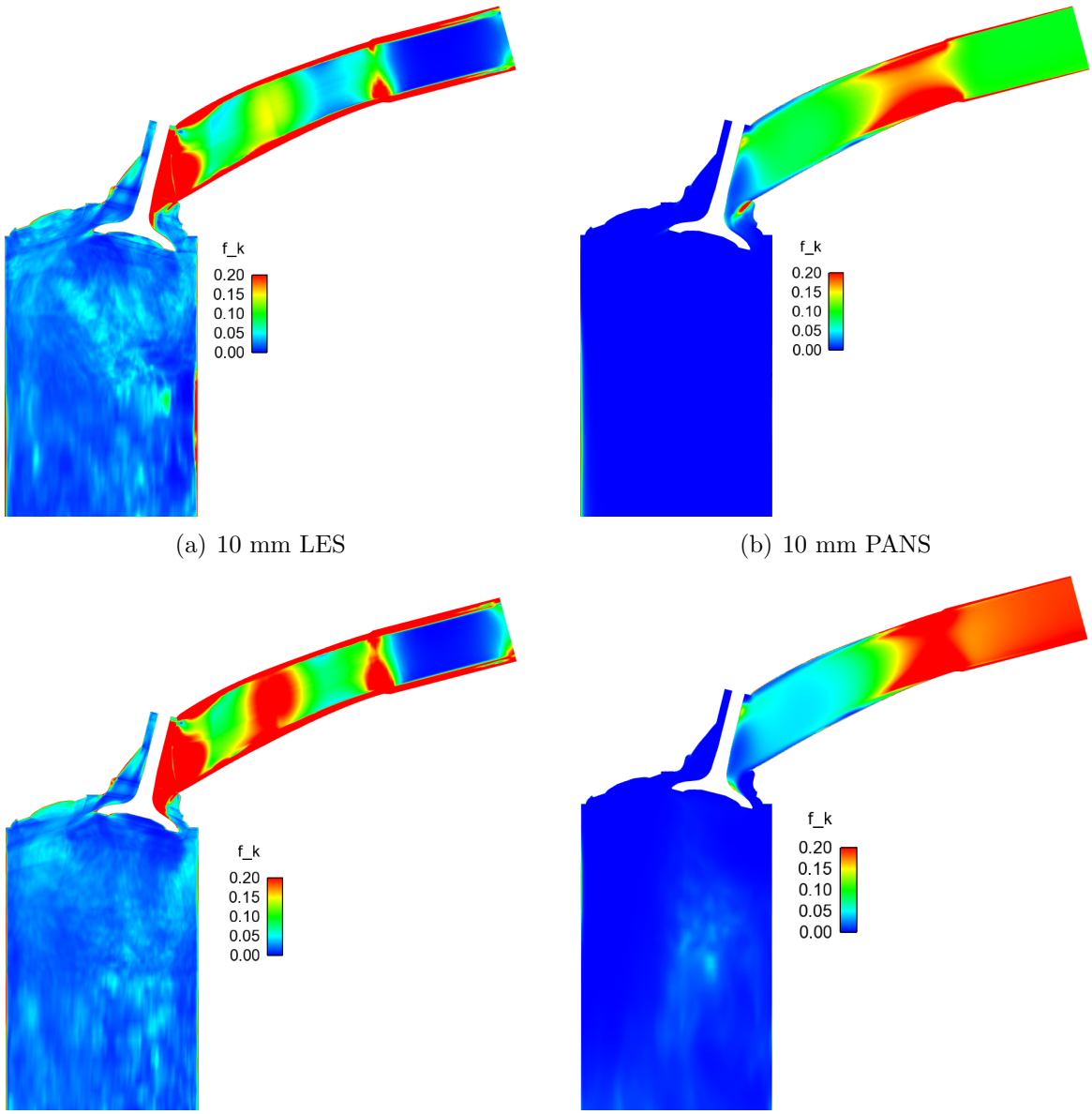

(a) 10 mm LES

(b) 10 mm PANS

(c) 6 mm LES

(d) 6 mm PANS

Figure 4.4.1.3: Comparison of the averaged unresolved-to-total ratio of turbulent kinetic energy, $<k_u>/(<k_u>+<k_r>)$, between LES and PANS for both 10 and 6 mm.

Chapter 5

Discussion and Conclusions

A characterization of the flow physics in the intake port was made in section 4.2 where especially two vortex structures of interest were identified. This have a direct influence on the calculated torque around the x-axis and therefore also influence the volumetric tumble number.
It could be seen in section 4.1 that all methods predicts the near wall flow differently and thus also predicts the friction velocity u^* different.
When working on such a complex geometry as the engine part in this study it might be too inefficient, time wise, to create a fully structured hexahedral mesh with blocking. A large part of the study was spent on the creation of the mesh and there was not enough time to create the mesh for the third case where the invalve valve lift is at 2 mm. It is however believed that this technique creates a high quality mesh well suited for demanding simulations such as LES.
It was seen in this study that the resolution requirements for LES were hard to fulfill. In order to run a LES that completely resolves the invalve the minimum mesh size is estimated to 64 million cells using the present blocking topology. Therefore it is believed that PANS can be a more suitable method for this case. Previous results has showed that PANS can predict the flow better than LES on a coarse mesh [3, 10, 11]. More rigorous validation of PANS is still required in order to use it as a reliable method. Therefore more experimental measurements on this geometry would be desirable in order to compare the predicted flow of a PANS simulation. Oil flow visualized photographs around all walls would for instance be useful in order to compare predicted flow structures and separations. It would also be desirable to get experimental estimations of the inlet turbulent flow conditions to make the PANS model as physical as it possibly can be.

Since there are only two experimental quantities to compare the simulations with, it is difficult to make strong conclusions about the predicted flows in this study. The isentropic flow cross-section area is a relatively simple variable which only depend on the mass flow rate at the inlet and the averaged pressure in the cylinder. Therefore it is not unexpected that the result of the simulations in all cases agree fairly well with the experimental data. As can be seen in figure 4.3.1.1 the closest predictions of this variable to the experimental data was achieved in the LES simulations.
The volumetric tumble number is defined by an equation strongly dependent on how the flow behaves in the cylinder. As can be seen in figure 4.3.2.1, none of the simulations predict this variable any way near the experimental data. The predictions are however close to each other and consistent with previous simulations in the benchmark study. One can only speculate in the reason for these differences with the current information. To understand these differences more detailed experimental data would be needed, for instance it would be

useful with all the measured parameters used in the equation for calculating the volumetric tumble number. As can be seen in section 4.1, a low torque value does not have to imply that there is no rotation in the cylinder. Instead it can also mean that two opposite rotations cancel each other. Therefore no conclusion can be made if the rotation with a positive effect on the torque is too low or if the rotation with a negative effect on the torque is too high.

5.1 Further work

As mentioned in section 4.1, the resolution for LES is not quite good enough. It was roughly estimated that a mesh of at least 64 million cells would be needed in order to fulfill the resolution requirements for LES at the invalve. Furthermore, no mesh independency study was made, both a coarser and finer mesh would be appropriate. Most importantly though, a more thorough investigation of the effect of the turbulent kinetic energy specified on the inlet in the PANS model needs to be done. Especially the inlet conditions in terms of turbulent kinetic energy needs to be estimated on a more physical basis.

Bibliography

[1] Picture of swirl and tumble. http://upload.wikimedia.org/wikipedia/commons/7/74/Swirl_and_Tumble.svg, 2013.

[2] Basara. B, Krajnović. S, Girimaji. S. PANS vs. LES for Computations of the Flow Around a 3D Bluff Body. *7th International ERCOFTAC Symposium on "Engineering Turbulence Modelling and Measurements"*, 2008.

[3] Basara. B, Krajnović. S, Girimaji. S. Pans methodology applied to elliptic-relaxation based eddy viscosity transport model. *Turbulence and Interactions, Notes on Numerical Fluid Mechanics and Multidisciplinary Design*, 110:63–69, 2010.

[4] L Davidsson. Fluid mechanics, turbulent flow and turbulence modeling. pages 131–138, 2013.

[5] P.A Durbin. Near-wall turbulence closure modelling without "damping functions". *Theoretical and Computational Fluid Dynamics*, 3:1–13, 1991.

[6] S Girimaji. Partially-averaged navier-stokes model for turbulence: A reynolds-averaged navier-stokes to direct numerical simulation bridging method. *ASME Journal of Applied Mechanics*, 73:413–421, 2006.

[7] BMW Group. Stationary flow bench 1. 2011.

[8] Hanjalić, K., Popovac, M., Hadziabdić, M. A robust near-wall elliptic-relaxation eddy-viscosity turbulence model for CFD. *International Journal of Heat and Fluid Flow*, 25:1047–1051, 2004.

[9] Dr. A. Kleemann. Stationary flow bench comparisons. 2011.

[10] Krajnović. S, Lárusson. R, Basara. B. Superiority of pans compared to les in predicting a rudimentary landing gear flow with affordable meshes. *International Journal of Heat and Fluid Flow*, 37:109–122, 2012.

[11] Krajnović. S, Ringqvist. P, Basara. B. Comparison of partially averaged navier-stokes and large-eddy simulations of the flow around a cuboid influenced by crosswind. *Journal of Fluids Engineering*, 134, 2012.

[12] Spalart Philippe R. Young-person's guide to detached-eddy simulation grids. *Technical Report*, 2001.

[13] J Smagorinsky. General circulation experiments with the primitive equations. *Montly Weather Review*, 91:99–165, 1963.